

Synchrotron-Based Time-Resolved X-ray Solution Scattering (Liquidography)

Shin-ichi Adachi¹, Jeongho Kim² and Hyotcherl Ihee²

¹*Photon Factory, High Energy Accelerator Research Organization, 1-1 O-ho, Tsukuba, Ibaraki 305-0801,*

²*Center for Time-Resolved Diffraction, Department of Chemistry and Graduate School of Nanoscience & Technology (WCU), KAIST, 305-701,*

¹*Japan*

²*Republic of Korea*

1. Introduction

Visualizing molecular structures in the course of a reaction process is one of the major grand challenges in chemistry, biology and physics. In particular, most chemical and biologically relevant reactions occur in solution, and solution-phase reactions exhibit rich chemistry due to the solute-solvent interplay. Studying photo-induced reactions in the solution phase offers opportunities for understanding fundamental molecular reaction dynamics and interplay between the solute and the solvent, but at the same time the interactions between solutes and solvents make this task challenging. Ultrafast emission, absorption and vibration spectroscopy in ultraviolet, visible and infrared regions have made possible the investigation of fast time-evolving processes. However, such time-resolved optical spectroscopic tools generally do not provide direct and detailed structural information such as bond lengths and angles of reaction intermediates because the spectroscopic signals utilizing light in the ultraviolet to infrared range cannot be directly translated into a molecular structure at the atomic level. In contrast, with the advance of X-ray synchrotron sources that can generate high-flux, ultrashort X-ray pulses, time-resolved X-ray diffraction (scattering) and absorption techniques have become general and powerful tools to explore structural dynamics of matters. Accordingly, the techniques have been successfully applied to studying various dynamics of chemical and biological systems (Coppens, 2003; Coppens *et al.*, 2004; Ihee, 2009; Ihee *et al.*, 2005b; Kim *et al.*, 2002; Schotte *et al.*, 2003; Srajer *et al.*, 1996; Techert *et al.*, 2001; Tomita *et al.*, 2009) and of condensed matters (Cavalleri *et al.*, 2005; Cavalleri *et al.*, 2006; Collet *et al.*, 2003; Fritz *et al.*, 2007; Gaffney *et al.*, 2005; Lee *et al.*, 2005; Lindenberg *et al.*, 2005). On one hand, time-resolved X-ray diffraction enables us to access to the mechanism of structural transformations at the atomic level in crystalline state (Collet *et al.*, 2003; Schotte *et al.*, 2003; Srajer *et al.*, 1996; Techert *et al.*, 2001). On the other hand, time-resolved X-ray absorption fine structure (XAFS) (Chen *et al.*, 2001; Saes *et al.*, 2003; Sato *et al.*, 2009) and time-resolved solution scattering (Davidsson *et al.*, 2005; Ihee, 2009; Ihee *et al.*, 2005a; Plech *et al.*, 2004) can probe structural dynamics in non-crystalline states of materials, complementing the X-ray diffraction technique.

In particular, time-resolved X-ray liquidography (TRXL), which is also known as time-resolved X-ray solution scattering (TRXSS), provides rather direct information of transient molecular structures because scattering signals are sensitive to all chemical species present in the sample and can be compared with the theoretical scattering signal calculated from three-dimensional atomic coordinates of involved chemical species. Accordingly, time-resolved X-ray liquidography using 100-picosecond X-ray pulses from a synchrotron source has been effective in elucidating molecular geometries involved in photoinduced reaction pathways, elegantly complementing ultrafast optical spectroscopy (Cammarata *et al.*, 2008; Cammarata *et al.*, 2006; Christensen *et al.*, 2009; Davidsson *et al.*, 2005; Georgiou *et al.*, 2006; Haldrup *et al.*, 2009; Ichiyangi *et al.*, 2009; Ihee, 2009; Ihee *et al.*, 2005a; Kim *et al.*, 2006; Kong *et al.*, 2008; Kong *et al.*, 2007; Lee *et al.*, 2008a; Lee *et al.*, 2006; Lee *et al.*, 2008b; Plech *et al.*, 2004; Vincent *et al.*, 2009; Wulff *et al.*, 2006).

Time-resolved X-ray liquidography has been developed by combining the pulsed nature of synchrotron radiation and of lasers. In a typical experiment, a reaction is initiated by an ultrashort optical laser pulse (pump), and the time evolution of the induced structural changes is probed by the diffraction of a time-delayed, short X-ray pulse as a function of the time delay between the laser and X-ray pulses. In other words, the X-ray pulse replaces the optical probe pulse used in time-resolved optical pump-probe spectroscopy. X-ray pulses with a temporal duration of 50 ~ 150 ps are generated by placing an undulator in the path of electron bunches in a synchrotron storage ring.

In this chapter, we aim to review the experimental details and recent applications of time-resolved X-ray liquidography. Especially, we describe the details of the TRXL setup in NW14A beamline at KEK, where polychromatic X-ray pulses with an energy bandwidth of $\Delta E/E \sim 1 - 5\%$ are generated by reflecting white X-ray pulses ($\Delta E/E = 15\%$) through multilayer optics made of W/B₄C or depth-graded Ru/C on silicon substrates. Unlike in conventional X-ray scattering/diffraction experiments, where monochromatic X-rays are used to achieve high structural resolution, polychromatic X-ray pulses containing more photons than monochromatic X-ray pulses are used at the expense of the structural resolution because a higher signal-to-noise ratio is desirable in the TRXL experiment. In addition, we describe in detail the principle of synchronization between the laser and synchrotron X-ray pulses, which is one of the key technical components needed for the success of time-resolved X-ray experiments, and has been vigorously implemented in well-established experimental techniques using synchrotron radiation, such as diffraction, scattering, absorption and imaging. Finally, some examples of applications to various reaction systems ranging from small molecules to proteins are described as well.

2. Experimental

2.1 Optical-pump and X-ray-scatter scheme

In a typical TRXL experiment, an ultrashort optical laser pulse initiates photochemistry of a molecule of interest in the solution phase, and an ultrashort x-ray pulse from a synchrotron facility, instead of an ultrashort optical pulse used in the optical pump-probe experiment, is sent to the reacting volume to probe the structural dynamics inscribed on the time-resolved x-ray diffraction signals as a function of reaction time. TRXL data have been collected using an optical-pump and x-ray-probe diffractometer in the beamline ID09B at ESRF (Bourgeois *et al.*, 1996; Wulff *et al.*, 1997) and the beamline NW14A of PF-AR at KEK (Nozawa *et al.*, 2007). The beamline 14IDB at APS also has the capability of collecting TRXL data. The

experimental setup is schematically illustrated in Fig. 1. It comprises a closed capillary jet or open-liquid jet to supply the solution that are pumped by laser pulses and scatter X-rays, a pulsed laser system to excite the sample, a pulsed synchrotron source to produce ultrashort X-ray pulses to scatter from the sample, a synchronized high-speed chopper that selects single X-ray pulses, and an integrating charge-coupled device (CCD) area detector.

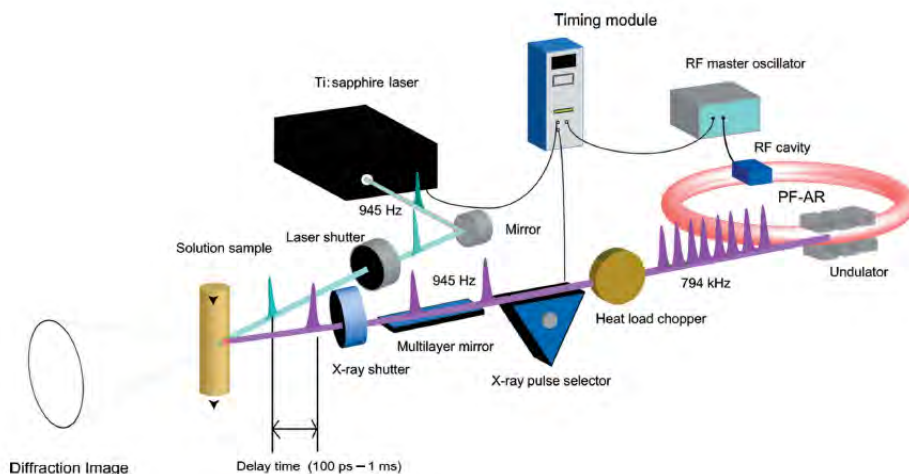


Fig. 1. Schematic drawing of the experimental setup for time-resolved X-ray liquidography. The liquid jet is irradiated by an optical laser pulse. After a well-defined time delay (t), the X-ray pulses generated by a synchrotron and selected by a high-speed chopper are sent to the sample and scatter. The reference diffraction data collected at -3 ns is subtracted from the diffraction data collected at positive time delays to extract the structural changes only.

2.2 Pulsed nature of synchrotron radiation

Synchrotron radiation is described as the radiation from charged particles accelerated at relativistic velocities by classical relativistic electrodynamics. It provides excellent characteristics as an X-ray source such as small divergence, short wavelength, linear or circular polarization, etc. Synchrotron radiation has another useful feature for time-resolved X-ray technique, short-pulsed nature, due to the periodic acceleration of charged particles in storage ring. Electrons circulating in storage ring irradiate synchrotron radiation and lose their energy. In order to compensate for the energy loss, a radio frequency (RF) oscillator accelerates electrons periodically at a harmonic frequency of the revolution frequency $f=c/L$, where c is the speed of light and L is the circumference of the storage ring. In order to keep electrons circulated stably in the storage ring, electrons need to pass through the RF oscillator at the appropriate timing, which is called the stable phase. Electrons stay and oscillate around the stable phase as a group, which is called electron bunch. Due to this equilibration process of the electron bunch, the length of the electron bunch is typically 15 – 45 mm (rms) that corresponds to X-ray pulse duration of 50 – 150 ps. Thus, the timing of the synchrotron X-ray pulse is synchronized with the timing of the RF oscillator. If the laser is externally triggered by the same RF master clock that accelerates electrons, both laser and X-ray pulses can be stably synchronized. This is the basis of time-resolved X-ray experiments using synchrotron radiation.

2.3 X-ray source characteristics and isolation of a single X-ray pulse

Synchrotron radiation is operated at MHz to GHz repetition rate depending on the bunch-filling modes of the storage ring. In particular, time-resolved experiments at synchrotron radiation facilities primarily require sparse bunch-filling mode of the storage ring operation such as single-bunch or hybrid modes. In general, X-ray detectors have a relatively slow response time and, furthermore, two-dimensional X-ray area detectors (e.g. CCD) have no fast gating capabilities. Due to such limitation of X-ray detectors, isolation of a single X-ray pulse from a pulse train is crucial for the success of time-resolved X-ray experiments. Since a single pulse can be readily isolated by using a fast chopper in sparse bunch-filling mode, the operation in the single-bunch or hybrid mode is highly desirable for time-resolved X-ray experiments.

The 6.5 GeV PF-AR is fully operated in a single-bunch mode for about 5000 hours/year. Electrons with a ring current of 60 mA (75.5 nC per bunch) are stored in a single electron bunch with a life time of around 20 hours. The RF frequency and harmonic number of the PF-AR are 508.58 MHz and 640, respectively. Therefore, the X-ray pulses are delivered at a frequency of 794 kHz ($= 508.58 \text{ MHz} / 640$) with a pulse duration of about 60 ps (rms). A schematic drawing of the beam line NW14A is shown in Fig. 2.

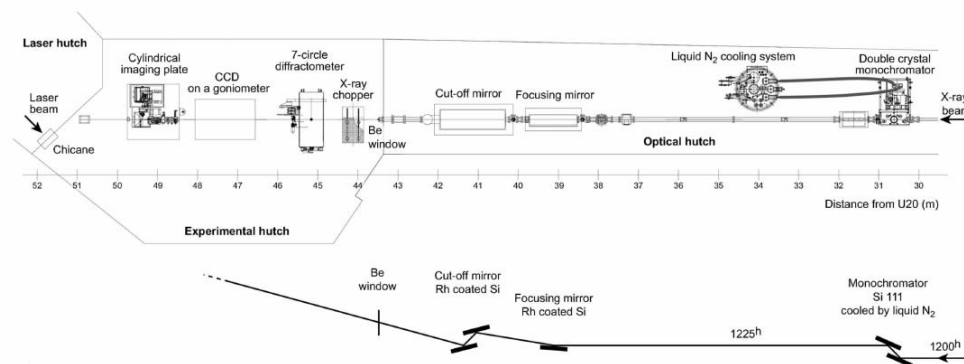


Fig. 2. Schematic drawing of the beamline NW14A of PF-AR at KEK. The X-ray beam is monochromized by a double-crystal monochromator and then focused using a bent-cylindrical mirror. Higher-order harmonics are cut off by a pair of flat mirrors.

The beam line has two undulators with a period length of 20 mm (U20) and 36 mm (U36). The U20 gives the 1st harmonic in the energy range of 13–18 keV. The energy bandwidth of the 1st harmonic is $\Delta E/E = 15\%$, which is utilized as a narrow-bandwidth white beam for TRXL experiments. The U36 covers an energy range of 5–20 keV with 1st, 3rd, and 5th harmonics, and useful for X-ray spectroscopy experiments. The measured photon flux from U36 and U20 at several gaps is shown in Fig. 3.

In order to isolate a single X-ray pulse from the sources, double X-ray choppers are equipped at the NW14A. The first chopper, called as heat-load chopper, has an opening time of 15 μs and is used to isolate 10-pulse train at 945 Hz (Gembicky *et al.*, 2007). The second X-ray chopper, made by Forschungszentrum Jülich (Lindenau *et al.*, 2004), consists of a rotor furnished with a narrow channel for the beam passage and isolates a single X-ray pulse from the 10-pulse train. The Jülich chopper realizes continuous phase locking with timing jitter less than 2 ns. The opening time of the channel at the center of the tapered aperture is

1.64 μs . If the repetition frequency of the pump-probe experiment is lower than 945 Hz, as is the case of using 10-Hz YAG laser system, a millisecond X-ray shutter (UNIBLITZ, XRS1S2P0) is set up between the X-ray chopper and the sample.

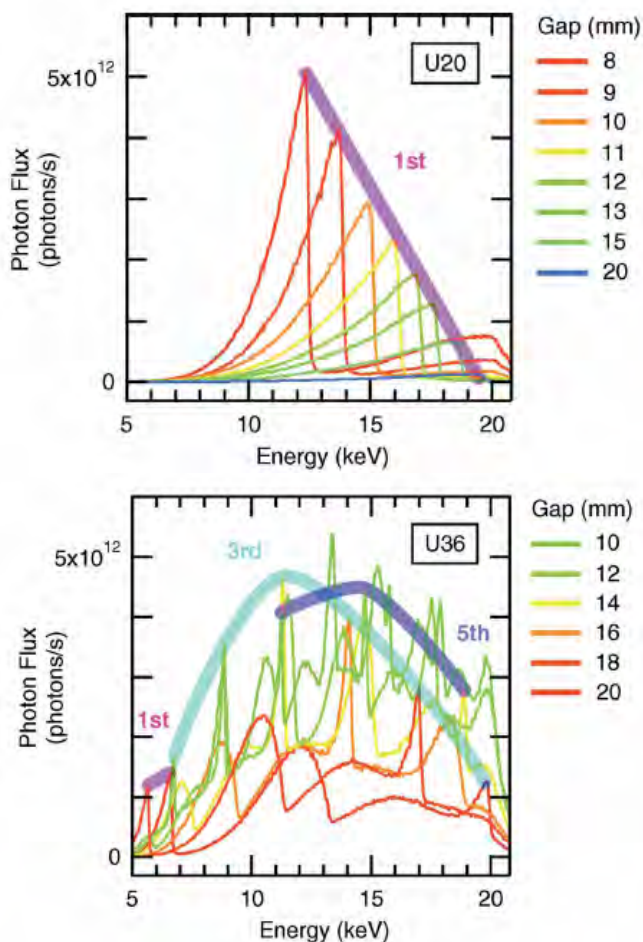


Fig. 3. Measured photon flux from U20 and U36 at several gaps. The intensity was normalized by 60 mA of the ring current and $0.318 \text{ mrad (H)} \times 0.053 \text{ mrad (V)}$ beam divergence.

2.4 Energy bandwidth of the incident X-ray beam

In order to gain maximum X-ray photon flux at 1 kHz repetition rate, energy bandwidth of the incident X-ray is the key issue. The X-ray pulse with 3% energy bandwidth of the first harmonics of the undulator has been used for TRXL experiments in the beamline ID09B at ESRF (Cammarata *et al.*, 2008; Cammarata *et al.*, 2006; Christensen *et al.*, 2009; Davidsson *et al.*, 2005; Georgiou *et al.*, 2006; Ichiyangi *et al.*, 2009; Ihee, 2009; Ihee *et al.*, 2005a; Kim *et al.*, 2006; Kong *et al.*, 2008; Kong *et al.*, 2007; Lee *et al.*, 2008a; Lee *et al.*, 2006; Lee *et al.*, 2008b;

Plech *et al.*, 2004; Vincent *et al.*, 2009; Wulff *et al.*, 2006). For example, the structural dynamics of $C_2H_4I_2$ in methanol were studied at the ID09B beamline (Ihee *et al.*, 2005a), and the reaction pathways and associated transient molecular structures in solution were resolved by the combination of theoretical calculations and global fitting analysis.

On the other hand, high-flux white X-ray at NW14A has $\Delta E/E = 15\%$ energy bandwidth when the undulator U20 is used due to relatively large electron beam emittance of PF-AR. In order to examine the feasibility of time-resolved liquidography with such a large bandwidth and to search for the optimal bandwidth, we simulated the Debye scattering curves for the reaction $C_2H_4I_2 \rightarrow C_2H_4I + I$ using (i) a 15% bandwidth with the default X-ray energy distribution, such as the undulator spectrum at the NW14A beamline, (ii) a Gaussian spectrum with a 5% bandwidth, (iii) a Gaussian spectrum with a 1% bandwidth, and (iv) a Gaussian spectrum with a 0.01% energy bandwidth, as shown in Fig. 4.

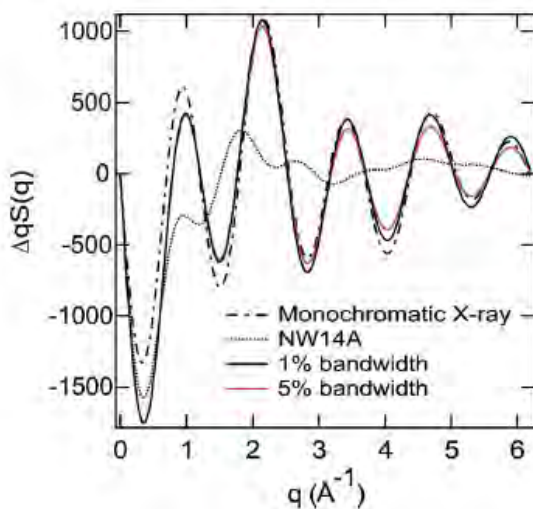


Fig. 4. Debye scattering curves calculated for the model reaction $C_2H_4I_2 \rightarrow C_2H_4I + I$ using a 0.01% (monochromatic) Gaussian X-ray energy profile (dot-dashed line), 5% Gaussian X-ray energy profile (red solid line), 1% Gaussian X-ray energy profile (solid line), and 15% default X-ray energy profile with a long tail (dotted line).

Although the photon flux of X-ray pulse increases with the energy bandwidth of the X-ray, the simulation shows that the default X-ray spectrum that has a 15% energy bandwidth as well as a long tail is not suitable for the time-resolved liquidography experiment owing to deteriorated structural resolution. Especially, the long tail of the default X-ray spectrum further blurs the scattering pattern at high scattering angles than when a symmetric Gaussian spectrum of the same bandwidth is assumed. As a result of the asymmetric lineshape, the X-ray spectrum with a long tail at ID09B of ESRF with a 3% bandwidth is effectively comparable to a symmetric Gaussian spectrum with a 10% bandwidth. In contrast, the scattering curve calculated from the Gaussian spectrum with a 5% energy bandwidth is similar in its structural resolution to that obtained from a 0.01% energy bandwidth (monochromatic) Gaussian spectrum. Furthermore, the total flux of the 5% energy bandwidth X-ray beam is higher than that of the monochromatic X-ray (a 0.01%

energy bandwidth) generated from a Si single crystal by a factor of 500. These estimations clearly suggest that the X-ray pulses with $\Delta E/E$ of 5% is appropriate for time-resolved X-ray liquidography experiment since it can provide a strong scattering signal without much sacrificing the structural resolution. Thus, we reduced the bandwidth of the X-ray pulses from the default 15% to less than the 5% energy bandwidth.

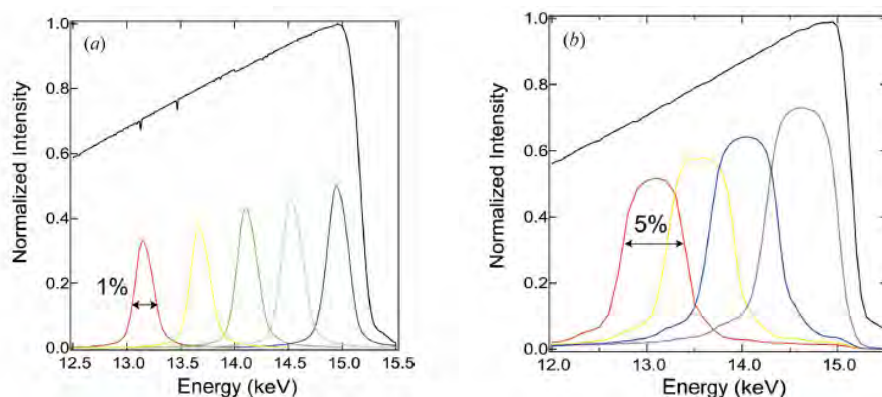


Fig. 5. Broadband X-ray pulses were produced by multilayer optics from the undulator spectrum. The peak energy position is controlled by changing the incident angle. The black curve is the X-ray spectrum from the undulator U20, with a gap of 11 mm. (a) X-ray spectra using the W/B₄C multilayer optics. The X-ray bandwidth is about 1%. (b) X-ray spectra using the depth-graded Ru/C multilayer optics. The X-ray bandwidth is 5%.

The multilayer optics produces X-ray pulses with a 1% to 5% energy bandwidth and allows us to measure TRXL with the undulator at the NW14A beamline. We used two types of multilayer optics. The first optics, made of W/B₄C ($d = 27.7$ Å, X-ray Company, Russia) on a Si single crystal with a size of $50 \times 50 \times 5$ mm³, provides an X-ray spectrum with a 1% energy bandwidth, as shown in Fig. 5(a). The peak energy of the X-ray spectrum can be changed by tilting the angle of the multilayer optics. The second multilayer optics, which is made of depth-graded Ru/C layer (average $d = 40$ Å, NTT Advanced Technology, Japan), produces a 5% energy bandwidth X-ray spectrum, as shown in Fig. 5(b). A white X-ray with a photon flux of 1×10^9 photons/pulse is produced at a 1 kHz repetition rate. When multilayer optics with 1% and 5% energy bandwidths are used at the downstream of the Jülich chopper, the photon flux of 6×10^7 and 3×10^8 photons/pulse is obtained, respectively.

2.5 Synchronization of laser and X-ray pulses

NW14A is equipped with a 150-fs Ti:sapphire regenerative amplifier laser system (Spectra Physics, Millennia, Tsunami, Spitfire, Empower). The Ti:sapphire laser system produces optical pulses at 800 nm at a 945-Hz repetition rate, with the pulse energy reaching up to 800 μJ/pulse. The laser is installed in a laser booth next to the experimental hutch. An optical parametric amplifier (Light Conversion, TOPAS-C) is also installed in the laser booth for conversion of 800 nm light to broad spectral range from visible to mid-infrared region. The laser beam is brought to the sample in the experimental hutch through a beam duct for the laser. The synchronization of X-ray and laser pulses is based on the RF master clock, by which an electron bunch is driven in the storage ring. When the X-ray experiment is

conducted with a 945 Hz Ti:sapphire-laser and a detector that has no gating capabilities (e.g. CCD), an X-ray chopper is required to synchronize the X-ray and laser pulses at a 1:1 ratio. The timing chart of the synchronization is shown in Fig. 6.

The X-ray pulse is emitted every $1.26 \mu\text{s}$ ($794 \text{ kHz} = 508 \text{ MHz} / 640$) from the PF-AR. After the RF amplifier, the RF master clock signal of PF-AR is split into two major timing components: one for the laser system and the other for the X-ray chopper system. In the X-ray chopper system, the 508 MHz RF and the 794 kHz revolution signals are used as the clock and the reference signals, respectively. A 945 Hz ($794 \text{ kHz} / 840$) repetition frequency of the X-ray pulses is then selected to trigger the Ti:sapphire 150-fs laser system running at the same repetition frequency. In the laser system, the mode-locked Ti:sapphire oscillator operating at 85 MHz ($508 \text{ MHz} / 6$) synchronized with the X-ray pulses provides seed pulses to the regenerative amplifier. The seed pulses trigger the regenerative amplifier pumped by the Q-switched Nd:YLF laser at 945 Hz ($85 \text{ MHz} / 89600$). Then, 945 Hz laser pulses are directed to the sample position by a series of mirrors. The pulse trains of pumping laser and probing X-ray pulses at the sample are shown together in Fig. 6. The timing of the delay between the two pulse trains is controlled by changing the ejection timing of the laser pulses from the regenerative amplifier using a phase shifter (Candox). The timing of the X-ray and the laser is measured with an InGaAs metal-semiconductor-metal (MSM) photodetector (Hamamatsu, G7096) coupled to a high-frequency preamplifier and a 2.5 GHz digital oscilloscope (Tektronix, DPO7254). The rise time of the MSM photodetector is typically 40 ps, which is faster than the X-ray pulse duration, and the photodetector is set at the sample position.

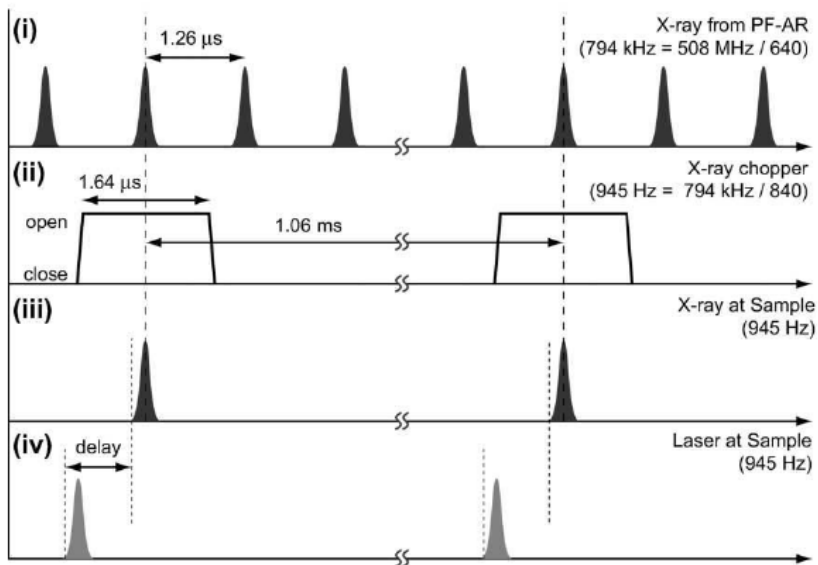


Fig. 6. The timing chart of the synchronization system at NW14A when using the X-ray chopper to synchronize 794 kHz X-ray and 945 Hz laser pulses at a 1:1 ratio. Timing settings of the X-rays from (i) PF-AR, (ii) the X-ray chopper, (iii) the X-rays at the sample, and (iv) the laser at the sample are shown.

2.6 Spatial and temporal overlaps

In order to increase the signal-to-noise ratio of the TRXL data and define accurate time delay between laser and X-ray pulses, the laser and X-ray pulses have to be overlapped at the sample both spatially and temporally. To check the temporal overlap, we place a fast InGaAs detector at the sample position and record the time traces of the laser and X-ray pulses along a single time axis monitored by a 2.5 GHz digital oscilloscope. By adjusting the laser firing time, it is possible to adjust the relative timing between the two pulses within a few picoseconds. During an experiment, the time traces of the laser and X-ray pulses are monitored by fast photodiodes simultaneously and non-intrusively.

The spatial overlap between X-ray and laser pulses is achieved by using a 50 μm diameter pinhole placed at the sample position. The pinhole is located at the center of X-ray beam, and then the laser beam is moved across the pinhole by scanning the position of the focusing lens until it passes through the center of the pinhole. To ensure precise spatial overlap, we monitor the intensity of scattering induced by thermal expansion in a liquid solvent, which typically occurs in 1 μs with our beam sizes. Specifically, the ratio of scattered intensities in the inner and outer disks of the solvent signal is monitored. Once the sample expands, the solvent signal shifts to lower scattering angles, leading to the increase of low-angle scattering and the decrease of high-angle scattering. Therefore, the ratio between the inner and outer part of the solvent signal changes in proportion with the laser excitation. The X-ray beam is typically vertically 200 μm and horizontally 250 μm . The laser spot is of circular shape with a diameter of 300 – 400 μm .

2.7 Sample environment and data acquisition

Two different types of sample cell systems have been used: a diluted solution of 0.5–100 mM concentration or pure solvent is prepared and circulated through either a capillary or through an open-jet sapphire nozzle. Such flow systems provide a stable liquid flow of ~ 0.3 mm thickness at a speed ensuring the refreshment of probe volume for every laser pulse (typically ~ 3 m/s). In the capillary-based system, the solution is flowed through a quartz capillary of 0.3 mm diameter. In the open-jet system, the capillary is removed and the solution is passed between two flat sapphire crystals with a spacing of 0.3 mm (Kyburz), which produces a stable naked liquid sheet directly exposed to the laser/x-ray beams. The open-jet system producing a bare liquid jet has the advantage over the closed capillary system in terms that the scattering background arising from the glass material of the capillary is eliminated and thus the signal-to-noise-ratio substantially improves. The lower background also helps to enhance the accuracy of the normalization process. In addition, the capillary jet often encounters a problem that the excitation laser drills a hole in the capillary. The molecules in the jet are excited by laser pulses from the femtosecond laser system described above. To maximize the population of transients and photoproducts, the laser pulse energy (typically 25 – 100 μJ depending on the excitation wavelength) is set to be relatively higher than that used in typical time-resolved optical spectroscopy, and thus multi-photon excitation often occurs. In general, one wants to follow photochemistry induced by only one-photon absorption that the laser pulse duration of ~ 100 fs is stretched to ~ 2 ps by introducing chirp from a pair of fused-silica prisms inserted before the sample. To probe slow photoinduced dynamics, a nanosecond laser system is used instead of the femtosecond laser system.

The laser beam is generally directed to the sample with a 10 degree tilt angle relative to the X-ray beam. The scattered X-ray diffraction signal is recorded by an area detector

(MarCCD165, Rayonics, 2048×2048 , $\sim 80 \mu\text{m}$ effective pixel size) with a sample-to-detector distance of $\sim 45 \text{ mm}$. A typical exposure time is $\sim 5 \text{ s}$, and, given the $\sim 1 \text{ kHz}$ repetition rate of the laser/X-ray pulses, the detector receives 5×10^3 X-ray pulses and $\sim 5 \times 10^{12}$ X-ray photons per image. Diffraction data are collected for typically 10 or more time-delays (t) from -100 ps up to $1 \mu\text{s}$ (for example, -100 ps , 0 ps , 30 ps , 100 ps , 300 ps , 1 ns , 3 ns , 10 ns , 30 ns , 100 ns , 300 ns , and $1 \mu\text{s}$). Each time-delay is interleaved by a measurement of the unperturbed sample (typically at -3 ns).

3. Data processing and analysis

3.1 Conversion of 2D images into 1D curves

The two-dimensional diffraction images are radially integrated into one-dimensional intensity curve, $S(q, t)^{exp}$, as a function of the momentum transfer q ($q = (4\pi/\lambda)\sin(2\theta/2)$ where λ is the wavelength of the X-rays, 2θ is the scattering angle, and t is the time delay). The curves are averaged and normalized by scaling them to absolute scale of the total (elastic and inelastic) scattering from one solution unit-cell molecule in the isosbestic point at high q values, where the scattering is insensitive to structural changes. After normalization, the diffraction data for the unperturbed sample measured at a negative time delay (typically at -3 ns) is subtracted from the diffraction data collected at positive time delays to extract the diffraction change only. The difference diffraction intensities $\Delta S(q, t)$ contain direct information on the structural changes of the solute and solvent in the probed solution. The relative laser induced diffraction signal change $\Delta S/S$ is quite small. It depends on both time and scattering angle, and is typically less than 0.1% . Standard deviations as a function of q are calculated in the process of conversion from a 2D image to a 1D curve by taking into account the distribution of the intensities at the same q value. The error of the averaged $\Delta S(q, t)$ can be obtained from the error propagation of standard deviations or by taking another standard deviation from the mean value of individual difference curves. The signal-to-noise ratio of a typical $\Delta S(q, t)$ depends on q and t and oscillates resembling the shape of $\Delta S(q, t)$ except that the negative values of $\Delta S(q, t)$ become positive in the plot of signal-to-noise ratio. A typical averaged $\Delta S(q, t)$ from about 50 - 100 repetitions has a signal-to-noise ratio up to 15. The signal-to-noise ratio is zero when ΔS is zero and reaches a maxima in the peaks and valleys of $\Delta S(q, t)$. To magnify the oscillatory feature at high q , $\Delta S(q, t)$ is often multiplied by q to yield $q\Delta S(q, t)$. Although $q\Delta S(q, t)$ contains direct information on the structural changes, often the result in reciprocal space is not intuitive. For this reason $q\Delta S(q, t)$ is transformed to real space where the changes are more readily interpretable: positive and negative peaks means formation and depletion, respectively, of the corresponding interatomic distance. Obtained through sine-Fourier transforms of $q\Delta S(q, t)$, the difference radial distribution function ($r\Delta R(r, t)$) represents the experimental atom-atom pair distribution function during the course of the reaction.

$$r\Delta R(r, t) = \frac{1}{2\pi^2} \int_0^\infty q\Delta S(q, t) \sin(qr) \exp(-q^2\alpha) dq \quad (1)$$

where the constant α is a damping constant to account for the finite experimental q range. In principle, the errors in the r -space can be also obtained from the same procedure as the one described for the q -space data: The sine-Fourier transform of every single $q\Delta S(q, t)$ is taken and then averaged over all $r\Delta R(r, t)$ curves, which defines a meaningful standard deviation.

3.2 Data analysis

We fit the experimental difference intensities ($\Delta S(q,t)^{exp}$) for all time delays against theoretical difference intensities ($\Delta S(q,t)^{theory}$), including the changes from three principal components that are mutually constrained by energy conservation in the X-ray illuminated volume: (i) the solute-only term, (ii) the solute-solvent cross term (also called as the cage term), and (iii) the solvent-only term from hydrodynamics as in the following expression.

$$\begin{aligned} \Delta S(q,t)^{theory} &= \Delta S(q,t)_{solute-only} + \Delta S(q,t)_{solute-solvent} + \Delta S(q,t)_{solvent-only} \\ &= \Delta S(q,t)_{solute-related} + \Delta S(q,t)_{solvent-only} \\ &= \frac{1}{R} \left[\sum_k c_k(t) S_k(q) - S_g(q) \sum_k c_k(0) \right] + (\partial S / \partial T)_\rho \Delta T(t) + (\partial S / \partial \rho)_T \Delta \rho(t) \end{aligned} \quad (2)$$

where R is the ratio of the number of solvent molecules to that of solute molecules, k is the index of the solute (reactants, intermediates and products), $c_k(t)$ the fraction of molecules in k as a function of time t , $S_k(q)$ is the solute-related (the solute-only plus the cage components) scattering intensity of species k , $S_g(q)$ is the scattering intensity of the reactants ($k = \text{reactants}$), $(\partial S(q) / \partial T)_\rho$ is the solvent scattering change in response to a temperature rise at constant volume, $(\partial S(q) / \partial \rho)_T$ is the response to a density change at constant temperature, $\Delta T(t)$ and $\Delta \rho(t)$ are the solvent temperature and density changes as a function of time. The equation indicates that, to calculate $\Delta S(q,t)^{theory}$, two types of basis components are needed: time-independent functions such as $S_k(q)$, $(\partial S(q) / \partial T)_\rho$ and $(\partial S(q) / \partial \rho)_T$ and time-dependent functions such as $c_k(t)$, $\Delta T(t)$ and $\Delta \rho(t)$. In the following, the steps involved in the calculation of time-independent and time-dependent basis functions are described with the photochemistry of CHI_3 in CH_3OH as an example. Fig. 7 presents an overall scheme for data analysis.

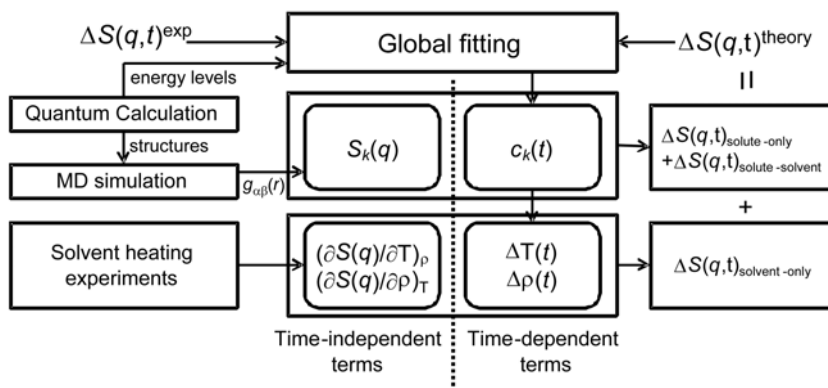


Fig. 7. Schematic of the data analysis. A theoretical difference scattering curve is represented as a sum of the three terms contributions: the solute-only term, the solute-solvent cross term, and the solvent-only term. The discrepancy between the theory and experiment is minimized in global fitting analysis by considering data at all positive time delays simultaneously. See the text for details.

$S_k(q)$ are calculated from MD simulations combined with quantum calculations. The possible structures of the parent molecule, the transient intermediates and the products in solution

are provided by fully optimizing the molecular geometry with the ab initio and/or density functional theory (DFT) methods with solvent effects included. In case of the photochemistry of CHI_3 in CH_3OH , the molecular structures of all putative species such as CHI_3 , CHI_2 , $\text{CHI}_2\text{-I}$ isomer, I_2 , I , and CH_3OH are calculated. The charge on each atom of all related species is also calculated via the natural bond orbital analysis. These structures and the charges of all species are used as starting points for the MD simulations, where one solute molecule is placed in a box containing 512 or more rigid solvent molecules. After MD simulations, pair correlation functions for atom pairs ($g_{\alpha\beta}(r)$ for the atom pair α and β) are calculated. The $S_k(q)$ curves are then computed by

$$S(q) = \sum_{\alpha\beta} f_{\alpha}(q) f_{\beta}(q) \left(N_{\alpha} \delta_{\alpha\beta} + \frac{N_{\alpha} N_{\beta}}{V} \int_0^{\infty} (g_{\alpha\beta}(r) - 1) \frac{\sin(qr)}{qr} 4\pi r^2 dr \right) \quad (3)$$

where $f_{\alpha}(q)$ is the atomic formfactor of the α atom, N_{α} is the number of α atoms in the MD simulation, $\delta_{\alpha\beta}$ is Kronecker delta, and V is the volume of the MD box. Including $g_{\alpha\beta}(r)$ for only the pairs within the solute molecule (for example, $\text{CHI}_2\text{-I}$ isomer has one type of $\text{C}\cdots\text{H}$, three types of $\text{C}\cdots\text{I}$, three types of $\text{H}\cdots\text{I}$ and three types of $\text{I}\cdots\text{I}$) results in the solute-only term, which can be also described by Debye scattering of isolated solute molecules as in the gas phase. The cage term is calculated when $g_{\alpha\beta}(r)$ for the solvent-solute cross pairs (for example, the CHI_2 radical in CH_3OH has $\text{C}_{\text{solute}}\cdots\text{C}_{\text{solvent}}$, $\text{C}_{\text{solute}}\cdots\text{O}$, $\text{I}\cdots\text{C}_{\text{solvent}}$, and $\text{I}\cdots\text{O}$, and many other pairs including H) are used in the integration. In practice, $g_{\alpha\beta}(r)$ for both solute-only and solute-solvent cross pairs are used to yield the solute-only plus cage terms, that is, the solute-related terms, $S_k(q)$. The solvent differential functions, $(\partial S(q)/\partial T)_p$ and $(\partial S(q)/\partial \rho)_T$, can be obtained either from MD simulations or determined in a separate experiment where the pure solvent is vibrationally excited by near-infrared light (Cammarata *et al.*, 2006). The latter gives superior agreement than the former. In general, the $g_{\alpha\beta}(r)$ from MD simulation for a particular atom pairs α and β can be used to calculate the contribution from that particular atom-atom pair to the overall signal, thereby aiding the peak assignment (for example, the atom pair of I and O gives the $\text{I}\cdots\text{O}$ interatomic contribution, which is one of the major solute-solvent cross terms).

The basic strategy of the least square fits to the experimental data is to minimize the total χ^2 iteratively in a global fitting procedure, simultaneously minimizing the differences between the experimental and theoretical curves at all positive time delays. The definition of chi-square (χ^2) used is as follows.

$$\chi^2 = \sum_t \chi_t^2 = \sum_t \sum_q \left(\frac{(\Delta S^{\text{theory}}(q,t) - \Delta S^{\text{exp}}(q,t))}{\sigma_{q,t}} \right)^2 \quad (4)$$

The polychromaticity of the X-ray beam has to be taken into account when a $\Delta S(q,t)^{\text{theory}}$ curve is compared with the $\Delta S(q,t)^{\text{exp}}$ curve by weighting the X-ray spectrum into the $\Delta S(q,t)^{\text{theory}}$ curve. A result of global fitting analysis for CHI_3 is shown in Fig. 8. The time-dependent basis functions ($c_k(t)$, $\Delta T(t)$ and $\Delta \rho(t)$) depend on the fitting parameters of the global fitting analysis. A set of rate equations for a reaction kinetic model including all reasonable candidate reaction pathways is set up to extract a reaction mechanism. As a candidate reaction model for CHI_3 , the rate constants for dissociation ($\text{CHI}_3 \rightarrow \text{CHI}_2 + \text{I}$), geminate and non-geminate recombination ($\text{CHI}_2 + \text{I} \rightarrow \text{CHI}_3$), and the non-geminate formation of

molecular iodine ($I + I \rightarrow I_2$) can be considered. Integrating the rate equations provides $c_k(t)$ to be used to construct the theoretical scattering signal. The $\Delta T(t)$ and $\Delta\rho(t)$ are mathematically linked to $c_k(t)$ and to each other by energy and mass conservation and hydrodynamics. From $c_k(t)$, the time-dependent heat released from solutes to the solvent, $Q(t)$, is calculated and used to compute $\Delta T(t)$ and $\Delta\rho(t)$ via thermodynamic and hydrodynamics relations (Bratos *et al.*, 2004).

The fitting parameters include the rate coefficients, the fraction of the excited molecules, the fraction of the molecules undergoing structural changes, and the laser beam size. Structural parameters such as bond lengths and angles and energy levels of chemical species can be included as fitting parameters.

3.3 Example: Photochemistry of CHI_3

Fig. 8A shows a comparison of $q\Delta S(q, t)^{exp}$ and $q\Delta S(q, t)^{theory}$ from global fitting analysis of TRXL data of CHI_3 in CH_3OH , and Fig. 8B shows the corresponding $r\Delta R(r, t)^{exp}$ and $r\Delta R(r, t)^{theory}$. Fig. 8E summarizes the final fit values. Upon irradiation of 20 mM iodoform in methanol, 24(\pm 1)% of the solute molecules are excited by the laser pulse at 267 nm. Among the excited iodoform, 28(\pm 1)% dissociate into $CHI_2 + I$ within the time resolution of 100 ps, and the remaining 72(\pm 1)% decay into the ground state via vibrational cooling and release their energy to the solvent. The iodine atoms recombine to form I_2 with the bimolecular rate constant of $1.55(\pm 0.25) \times 10^{10} \text{ M}^{-1}\text{s}^{-1}$. Based on these values from global fitting analysis, chemical population changes (as shown in Fig. 8C) and the temperature and density change of the solvent (as shown in Fig. 8D) as a function of time can be drawn. Initially, the temperature and the pressure of the solvent increase at a constant volume due to the energy transfer from the solute to solvent. Then, the thermal expansion occurs with a time constant of ~ 50 ns, returning the sample to ambient pressure. Due to the thermal expansion, the density of the solvent decreases by 1.2 kg/m^3 (0.15%) at 1 μs , leading to a temperature increase of 1.02 K. After the analysis, the whole signal can be decomposed into each component. For example, the solute-only term, the cage term, and the solvent-only term in real space are shown in Figs. 9D, 9E, and 9F along with the assignment of the peaks in the real space. The prominent negative peak around 3.6 \AA of the solute-only term (Fig. 9D) is due to the depletion of the I \cdots I distance in CHI_3 and the shoulder at 2.7 \AA in late time delays is due to the formation of a new I-I bond in I_2 . Most positive and negative peaks located at distances larger than the size of the solute molecule in Fig. 9E and 9F are related to the solvent rearrangement due to temperature and density changes.

4. Applications

4.1 On the issue of isomer formation from CHI_3 in methanol

TRXL has been used to capture the molecular structures of intermediates and their reaction kinetics for various photochemical processes. In the following, we present some application examples ranging from small molecules to proteins, which illustrate the wide applicability of TRXL.

The first example is the photochemistry of iodoform (CHI_3). According to previous time-resolved spectroscopic studies (Wall *et al.*, 2003; Zheng *et al.*, 2000), the CHI_2 radical and I atom generated upon excitation at 267 nm geminately recombine to form iso-iodoform within the solvent cage as the main species (quantum yield of at least 0.5) with a rise time of 7 ps and this iso-iodoform survives for up to microseconds. To investigate the possibility of

the isomer formation, we performed the global fitting analysis on the TRXL data with two candidate reaction pathways ($[\text{CHI}_3 \rightarrow \text{CHI}_2 + \text{I}; \text{simple dissociation channel}]$ and $[\text{CHI}_3 \rightarrow \text{CHI}_2\text{-I}; \text{isomer formation channel}]$). As shown in Fig. 8, the isomer channel reaction model is not compatible with the TRXL data, but a simple dissociation channel gives good agreement

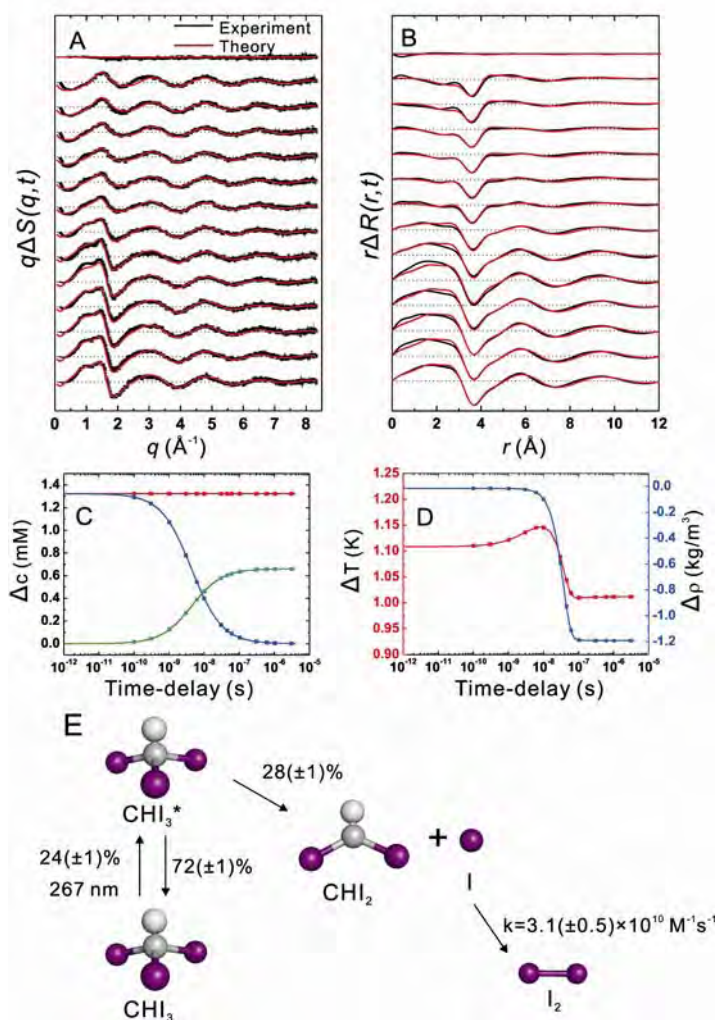


Fig. 8. Structural dynamics of the photochemistry of CHI_3 in methanol upon photolysis at 267 nm determined by TRXL. (A) Experimental difference-diffraction intensities, $q\Delta S(q, t)$ (black) and theoretical curves (red) as a result of global fitting analysis. (B) Difference radial distribution curves, $r\Delta R(r, t)$, corresponding to (A). (C) The population changes of the various chemical species as a function of time delay determined from global fitting analysis. (D) The change in the solvent density (red) and temperature (blue) determined from global fitting analysis. (E) A reaction mechanism determined by TRXL.

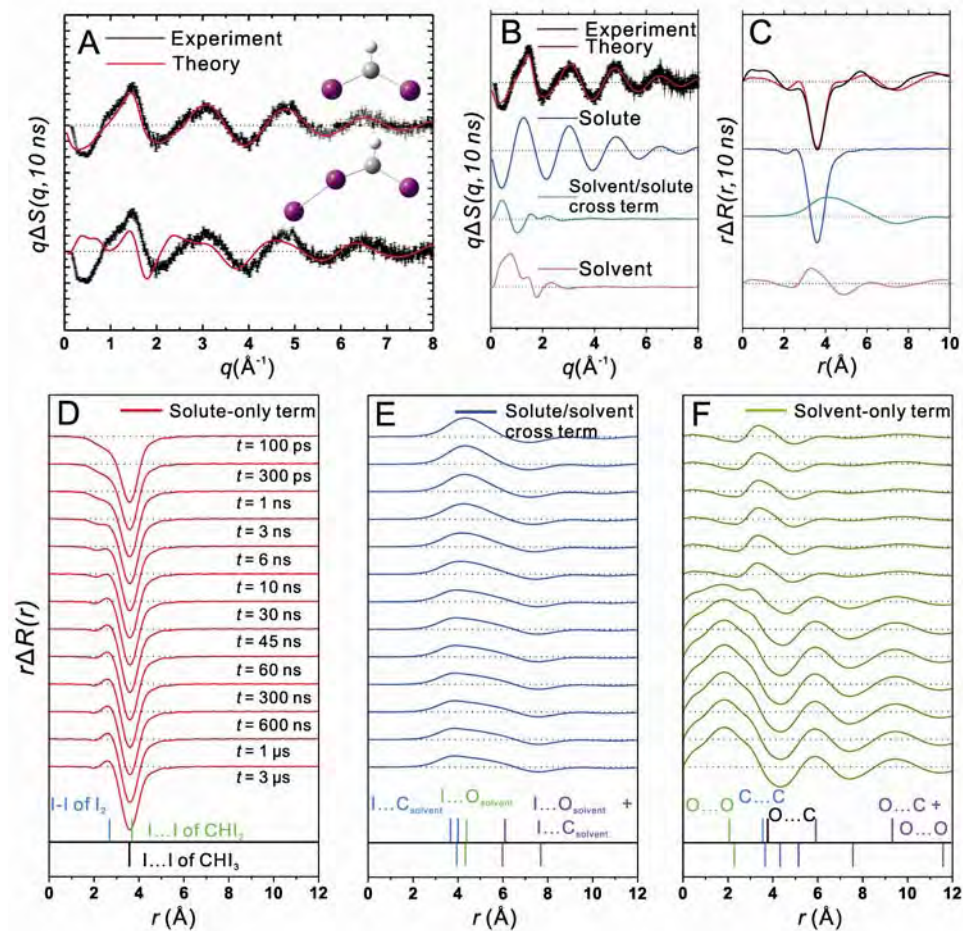


Fig. 9. Determining the major reaction channel for CHI_3 in methanol excited at 267 nm and decomposition into three components for peak assignment. (A) $q\Delta S(q, t)$ for two candidate reaction pathways, CHI_2 formation versus CHI_2 -I isomer formation, are compared. Experimental curves with experimental errors are shown in black and theoretical curves are in red. The CHI_2 formation channel gives superior agreement between experiment and theory, confirming that simple dissociation is the major reaction pathway and the isomer formation is negligible. (B) The $q\Delta S(q, 10 \text{ ns})$ curve is decomposed into the solute-only, cage, and solvent-only contributions. (C) The same decomposition in the real space for $r\Delta R(r, 10 \text{ ns})$ corresponding to (B). (D) The solute-only component of $r\Delta R(r, t)$. (E) The cage component of $r\Delta R(r, t)$. (F) The solvent-only component of $r\Delta R(r, t)$.

(Lee *et al.*, 2008a). Furthermore, when both reaction models are included in the fit, the fraction of the isomer-formation process converges to zero, confirming that the iso-iodoform should be a minor species if it forms at all. Since the X-ray pulse width used in this study is

~100 ps (fwhm), the formation of iso-iodoform as a major species on time scales shorter than our experimental time resolution cannot be ruled out. The subsequent kinetics obtained from TRXL was detailed in the previous section (Data Analysis). It should be noted that the data show that the formation of I_2 is dominant over other possible recombination products such as CHI_3 (from CH_3 and I) and C_2H_6 (from two CH_3).

4.2 Protein folding of cytochrome c

Protein structural changes in solution have been mainly characterized by time-resolved optical spectroscopic methods that, despite their high time resolution (<100 fs), are only indirectly related to three-dimensional structures in space. For protein crystals, a combination of high time resolution and structural sensitivity has become readily available with the advent of sub-nanosecond Laue crystallography (Ihee *et al.*, 2005b; Moffat, 2001; Schotte *et al.*, 2003; Srajer *et al.*, 1996), but its applicability has been limited to a few model systems due to the stringent prerequisites such as highly-ordered and radiation-resistant single crystals. More importantly, crystal packing constraints might hinder biologically relevant motions. Owing to such limitations, the time-resolved X-ray crystallography has been applied to only reversible reactions in single crystals, and it cannot be simply used to study irreversible reactions such as protein folding. To obtain information about protein motions in a more natural environment, X-ray scattering and nuclear magnetic resonance (NMR) methods have been mainly used as direct structural probes of protein structures in solution (Grishaev *et al.*, 2005; Schwieters *et al.*, 2003). Due to the inverse relationship between the interatomic distance and the scattering angle, the scattering from macromolecules is radiated at smaller scattering angles and is typically called as small-angle X-ray scattering (SAXS) or wide-angle X-ray scattering (WAXS) for scattering angles larger than conventional SAXS angles. The SAXS is sensitive to overall structure, for example, overall size and shape, of the protein, while wide-angle X-ray scattering (WAXS) gives more detailed information on the tertiary and quaternary structure such as the fold of helices and sheets. However, thus far, the time resolution had been limited to 160 μ s at best (Akiyama *et al.*, 2002). As well, NMR is a powerful technique for structure determination in solution, but it works best for small proteins and needs properly labeled samples (Kainosho *et al.*, 2006). More importantly, due to the nature of microwave pulses, the time resolution of protein NMR is inherently limited to milliseconds.

In case of protein solutions, the relatively low concentration (only a few mM or less) make TRXL measurements non-trivial, and the large molecular size of proteins (more than thousand times larger than small molecules) complicates the structural analysis. However, recent TRXL data from model proteins in solution have demonstrated that the medium to large-scale dynamics of proteins is rich in information on time scales from nanoseconds to milliseconds (Cammarata *et al.*, 2008). TRXL methodology has been applied to human haemoglobin (Hb), a tetrameric protein made of two identical $\alpha\beta$ dimers, that is known to have at least two different quaternary structures (a ligated stable "relaxed" (R) state and an unligated stable "tense" (T) structures) in solution. The tertiary and quaternary conformational changes of human hemoglobin triggered by laser induced ligand dissociation have been identified using the TRXL method. A preliminary analysis by the allosteric kinetic model gives a time scale for the R-T transition of ~1-3 μ s, which is shorter than the time scale derived with time-resolved optical spectroscopy. The optically induced tertiary relaxation of myoglobin (Mb) and refolding of cytochrome c (Cyt-c) have been also

studied with TRXL. As previously mentioned, the advantage of TRXL over time-resolved X-ray protein crystallography is that it can probe irreversible reactions as illustrated with the folding of cytochrome c as well as reversible reactions such as ligand reactions in heme proteins.

The basic idea of protein folding is that the three-dimensional structure of proteins is mainly determined by their amino acid sequences. Unfolded polypeptide chains use this information to accurately and quickly fold into their native structures (Fig. 10a). The optically triggered folding of horse heart Cyt-c has been extensively studied with spectroscopic techniques (Chen *et al.*, 1998; Jones *et al.*, 1993) and also by using fast-mixing SAXS (Akiyama *et al.*, 2002). Cyt-c is a single domain protein similar to Mb. Unlike Hb and Mb, Cyt-c does not usually bind external ligands such as CO since the iron atom of the heme group is covalently coordinated to the Met-80 residue of the protein. However, if Cyt-c is partially unfolded with a denaturing agent, it is possible to replace the Met-80 residue with CO and the CO ligand can be optically dissociated, thereby initiating the re-folding process. The time-dependent evolution of the TR-WAXS signal of Cyt-c after photolysis is evident, especially in the small-angle region (Fig. 10b). As a preliminary analysis, we fitted the observed signal as a linear combination of one pattern at the earliest time delay, 32 μ s, and

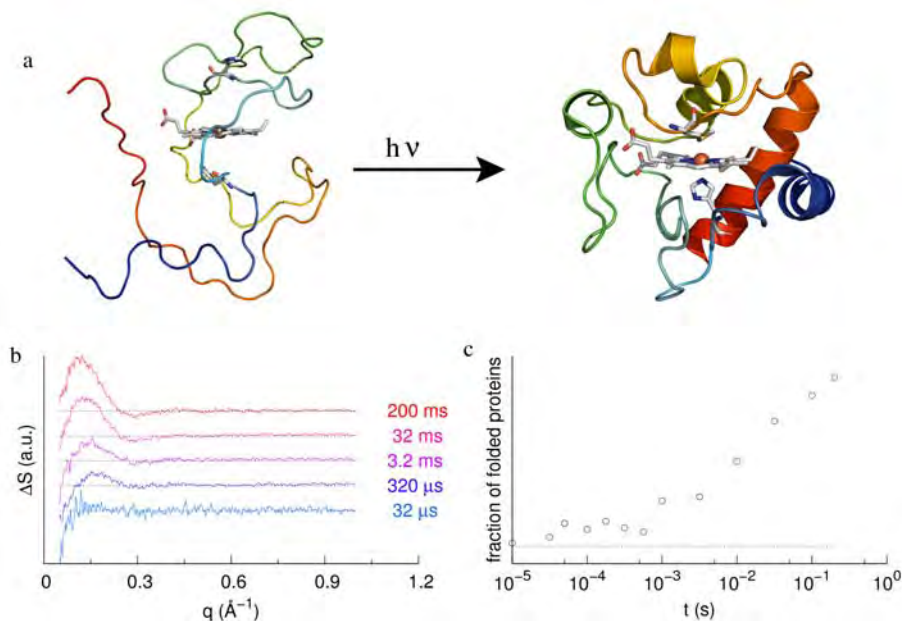


Fig. 10. Application of TRXL to track the folding of cytochrome c. (a) Schematic representation of light-induced folding of cytochrome c. (b) Time-resolved WAXS data relative to CO-photolysis-induced folding of cytochrome c. A 200 ns laser pulse at 532 nm was used to initiate photodissociation of the CO ligand, which in turn initiates the folding process. Experimental data at representative time delays are shown. (c) Population of the folded state as a function of time estimated from a linear combination of the experimental signal at 32 μ s and 0.2 s (open symbols). A simple exponential analysis yields a time constant of about 25 ms.

the other at the latest time delay, 0.2 s. This simple approach reproduces the experimental data at all times very well. The plot of the weighting factor of the late time component against time is shown in Fig. 10c and a simple exponential analysis yields a time scale of about 25 ms for the CO-photolysis-triggered folding.

5. Summary and future perspectives

In this chapter, we have described the principle and experimental details of TRXL technique with recent examples of its applications. With 100-ps X-ray pulses readily available from synchrotron radiation, TRXL has been established as a powerful tool for characterizing fast structural transition dynamics of chemical reactions and biological processes, ranging from small molecules to proteins in solution. In particular, the technique provides rather direct information on transient molecular structures since scattering signals are sensitive to all chemical species present in the sample unlike in the optical spectroscopy. Although there still remain challenges to overcome, for example, limited structural and time resolution, TRXL is expected to play an important role in revealing transient structural dynamics in many other systems in solution and liquid phases, especially with the aid of next-generation X-ray sources. At the frontier of the technical advances supporting such bright prospects of TRXL is the advent of linac-based X-ray light sources, which can generate X-ray pulses of femtosecond duration. They include self-amplified spontaneous emission X-ray free electron lasers (SASE-XFEL) and energy recovery linacs (ERL) that are currently under development will be available in the near future.

Among these novel X-ray sources, the high-gain XFEL using SASE promises to generate highly coherent, femtosecond X-ray pulses on the order of 100 fs with a high photon flux up to 10^{13} photons per pulse. The superb time resolution of XFEL will enable us to access reaction dynamics in femtosecond time regime, elucidating much more details of ultrafast structural dynamics. Also, the high flux of XFEL provides the potential for single-shot collection of the XFEL signal. On the other hand, ERL can be operated at a high repetition rate on the order of MHz to GHz. Such high repetition rate capability of ERL will be able to significantly improve the signal-to-noise ratio of TRXL signal since TRXL is basically a perturbative, pump-probe type experiment. With such a high-repetition rate X-ray source, TRXL can be implemented combined with a high-repetition rate oscillator instead of femtosecond amplified lasers, which is commonly operated at only a kHz rate. Furthermore, the nanometer-scale size of the X-ray beam from the ERL (typically 100-nm diameter) will allow tight focusing of the laser beam down to the order of micrometers, enabling the collection of signal from a small volume of sample. Since the scattering signal from the small area will be relatively weak, low-noise and fast-gatable two-dimensional detectors are desirable for future ERL-applied TRXL experiments. The development of pixel detectors using silicon-on-insulator technology will pave the way for such high-performance two-dimensional detectors.

The excellent beam characteristics of the ERL will be further extended to develop the coherent X-ray source, for example, oscillator-type XFEL (XFEL oscillator or XFEL-O) (Kim *et al.*, 2008). The X-ray source generating fully coherent X-ray pulses will serve as the ultimate X-ray light source with superb spatial and temporal coherence. Then, what kind of potential applications can we expect once fully coherent X-ray pulses become available? For example, by making an analogy to the ultrafast optical spectroscopy that fully takes advantage of the temporal coherence of ultrashort optical laser pulses, one could imagine

phase-coherent spectroscopy in the X-ray regime with controlled timing, phase, and intensity among multiple, coherent X-ray pulses (Mukamel *et al.*, 2009). As X-ray radiation has the sub-nm wavelength, which corresponds to the sub-attosecond period in the time domain, X-ray pulses offer much higher spatial and temporal resolution than achievable in the optical regime. Thus, the development of X-ray sources that can generate coherent X-ray pulses will revolutionize the whole X-ray science.

6. References

- Akiyama, S.; Takahashi, S.; Kimura, T.; Ishimori, K.; Morishima, I.; Nishikawa, Y. & Fujisawa, T. (2002). Conformational landscape of cytochrome c folding studied by microsecond-resolved small-angle x-ray scattering. *Proc. Nat. Acad. Sci.*, 99, 1329-1334.
- Bourgeois, D.; Ursby, T.; Wulff, M.; Pradervand, C.; LeGrand, A.; Schildkamp, W.; Laboure, S.; Srajer, V.; Teng, T.-Y.; Roth, M. & Moffat, K. (1996). Feasibility and realization of single-pulse Laue diffraction on macromolecular crystals at ESRF. *J. Synchrotron Rad.*, 3, 65-74.
- Bratos, S.; Mirloup, F.; Vuilleumier, R.; Wulff, M. & Plech, A. (2004). X-ray "filming" of atomic motions in chemical reactions. *Chem. Phys.*, 304, 245-251.
- Cammarata, M.; Levantino, M.; Schotte, F.; Anfinrud, P. A.; Ewald, F.; Choi, J.; Cupane, A.; Wulff, M. & Ihee, H. (2008). Tracking the structural dynamics of proteins in solution using time-resolved wide-angle X-ray scattering. *Nat. Methods*, 5, 881-886.
- Cammarata, M.; Lorenc, M.; Kim, T. K.; Lee, J. H.; Kong, Q. Y.; Pontecorvo, E.; Lo Russo, M.; Schiro, G.; Cupane, A.; Wulff, M. & Ihee, H. (2006). Impulsive solvent heating probed by picosecond x-ray diffraction. *J. Chem. Phys.*, 124, 124504.
- Cavaliere, A. L.; Fritz, D. M.; Lee, S. H.; Bucksbaum, P. H.; Reis, D. A.; Rudati, J.; Mills, D. M.; Fuoss, P. H.; Stephenson, G. B.; Kao, C. C.; Siddons, D. P.; Lowney, D. P.; MacPhee, A. G.; Weinstein, D.; Falcone, R. W.; Pahl, R.; Als-Nielsen, J.; Blome, C.; Dusterer, S.; Ischebeck, R.; Schlarb, H.; Schulte-Schrepping, H.; Tschentscher, T.; Schneider, J.; Hignette, O.; Sette, F.; Sokolowski-Tinten, K.; Chapman, H. N.; Lee, R. W.; Hansen, T. N.; Synnergren, O.; Larsson, J.; Techert, S.; Sheppard, J.; Wark, J. S.; Bergh, M.; Caleman, C.; Huldt, G.; van der Spoel, D.; Timneanu, N.; Hajdu, J.; Akre, R. A.; Bong, E.; Emma, P.; Krejčík, P.; Arthur, J.; Brennan, S.; Gaffney, K. J.; Lindenberg, A. M.; Luening, K. & Hastings, J. B. (2005). Clocking femtosecond x rays. *Phys. Rev. Lett.*, 94.
- Cavalleri, A.; Wall, S.; Simpson, C.; Statz, E.; Ward, D. W.; Nelson, K. A.; Rini, M. & Schoenlein, R. W. (2006). Tracking the motion of charges in a terahertz light field by femtosecond X-ray diffraction. *Nature*, 442, 664-666.
- Chen, E.; Wood, M. J.; Fink, A. L. & Kliger, D. S. (1998). Time-Resolved Circular Dichroism Studies of Protein Folding Intermediates of Cytochrome c. *Biochemistry*, 37, 5589-5598.
- Chen, L. X.; Jager, W. J. H.; Jennings, G.; Gosztola, D. J.; Munkholm, A. & Hessler, J. P. (2001). Capturing a Photoexcited Molecular Structure Through Time-Domain X-ray Absorption Fine Structure. *Science*, 292, 262-264.
- Christensen, M.; Haldrup, K.; Bechgaard, K.; Feidenhans'l, R.; Kong, Q. Y.; Cammarata, M.; Lo Russo, M.; Wulff, M.; Harrit, N. & Nielsen, M. M. (2009). Time-Resolved X-ray Scattering of an Electronically Excited State in Solution. Structure of the (3)A(2u) State of Tetrakis-mu-pyrophosphidodiplatinate(II). *J. Am. Chem. Soc.*, 131, 502-508.
- Collet, E.; Lemeec-Cailleau, M. H.; Buron-Le Cointe, M.; Cailleau, H.; Wulff, M.; Luty, T.; Koshihara, S. Y.; Meyer, M.; Toupet, L.; Rabiller, P. & Techert, S. (2003). Laser-induced ferroelectric structural order in an organic charge-transfer crystal. *Science*, 300, 612-615.

- Coppens, P. (2003). What can time-resolved diffraction tell us about transient species? excited-state structure determination at atomic resolution. *Chem. Comm.*, 1317-1320.
- Coppens, P.; Vorontsov, I.; Graber, T.; Kovalevsky, A. Y.; Chen, Y. S.; Wu, G.; Gembicky, M. & Novozhilova, I. V. (2004). Geometry changes of a Cu(I) phenanthroline complex on photoexcitation in a confining medium by time-resolved x-ray diffraction. *J. Am. Chem. Soc.*, 126, 5980-5981.
- Davidsson, J.; Poulsen, J.; Cammarata, M.; Georgiou, P.; Wouts, R.; Katona, G.; Jacobson, F.; Plech, A.; Wulff, M.; Nyman, G. & Neutze, R. (2005). Structural determination of a transient isomer of CH2I2 by picosecond x-ray diffraction. *Phys. Rev. Lett.*, 94, 245503.
- Fritz, D. M.; Reis, D. A.; Adams, B.; Akre, R. A.; Arthur, J.; Blome, C.; Bucksbaum, P. H.; Cavalieri, A. L.; Engemann, S.; Fahy, S.; Falcone, R. W.; Fuoss, P. H.; Gaffney, K. J.; George, M. J.; Hajdu, J.; Hertlein, M. P.; Hillyard, P. B.; Hoegen, M. H. V.; Kammler, M.; Kaspar, J.; Kienberger, R.; Krejcik, P.; Lee, S. H.; Lindenberg, A. M.; McFarland, B.; Meyer, D.; Montagne, T.; Murray, E. D.; Nelson, A. J.; Nicoul, M.; Pahl, R.; Rudati, J.; Schlarb, H.; Siddons, D. P.; Sokolowski-Tinten, K.; Tschentscher, T.; von der Linde, D. & Hastings, J. B. (2007). Ultrafast bond softening in bismuth: Mapping a solid's interatomic potential with X-rays. *Science*, 315, 633-636.
- Gaffney, K. J.; Lindenberg, A. M.; Larsson, J.; Sokolowski-Tinten, K.; Blome, C.; Synnergren, O.; Sheppard, J.; Coleman, C.; MacPhee, A. G.; Weinstein, D.; Lowney, D. P.; Allison, T.; Matthews, T.; Falcone, R. W.; Cavalieri, A. L.; Fritz, D. M.; Lee, S. H.; Bucksbaum, P. H.; Reis, D. A.; Rudati, J.; Macrander, A. T.; Fuoss, P. H.; Kao, C. C.; Siddons, D. P.; Pahl, R.; Moffat, K.; Als-Nielsen, J.; Duesterer, S.; Ischebeck, R.; Schlarb, H.; Schulte-Schrepping, H.; Schneider, J.; von der Linde, D.; Hignette, O.; Sette, F.; Chapman, H. N.; Lee, R. W.; Hansen, T. N.; Wark, J. S.; Bergh, M.; Hultdt, G.; van der Spoel, D.; Timneanu, N.; Hajdu, J.; Akre, R. A.; Bong, E.; Krejcik, P.; Arthur, J.; Brennan, S.; Luening, K. & Hastings, J. B. (2005). Observation of structural anisotropy and the onset of liquidlike motion during the nonthermal melting of InSb. *Phys. Rev. Lett.*, 95.
- Gembicky, M.; Adachi, S. & Coppens, P. (2007). A kHz heat-load shutter for white-beam experiments at synchrotron sources. *J. Synch. Rad.*, 14, 295-296.
- Georgiou, P.; Vincent, J.; Andersson, M.; Wohri, A. B.; Gourdon, P.; Poulsen, J.; Davidsson, J. & Neutze, R. (2006). Picosecond calorimetry: Time-resolved x-ray diffraction studies of liquid CH2Cl2. *J. Chem. Phys.*, 124, 234507.
- Grishaev, A.; Wu, J.; Trehella, J. & Bax, A. (2005). Refinement of multidomain protein structures by combination of solution small-angle X-ray scattering and NMR data. *J. Am. Chem. Soc.*, 127, 16621-16628.
- Haldrup, T.; Lemke, H. T.; Haldrup, K.; Nielsen, T. N.; Arms, D. A.; Walko, D. A.; Miceli, A.; Landahl, E. C.; Dufresne, E. M. & Nielsen, M. M. (2009). Picosecond time-resolved laser pump/X-ray probe experiments using a gated single-photon-counting area detector. *J. Synch. Rad.*, 16, 387-390.
- Ichiyanagi, K.; Sato, T.; Nozawa, S.; Kim, K. H.; Lee, J. H.; Choi, J.; Tomita, A.; Ichikawa, H.; Adachi, S.; Ihee, H. & Koshihara, S. (2009). 100-picosecond time-resolved solution scattering utilizing wide-bandwidth X-ray beam from multilayer optics. *J. Synch. Rad.*, 16, 391-394.
- Ihee, H. (2009). Visualizing Solution-Phase Reaction Dynamics with Time-Resolved X-ray Liquidography. *Acc. Chem. Res.*, 42, 356-366.
- Ihee, H.; Lorenc, M.; Kim, T. K.; Kong, Q. Y.; Cammarata, M.; Lee, J. H.; Bratos, S. & Wulff, M. (2005a). Ultrafast x-ray diffraction of transient molecular structures in solution. *Science*, 309, 1223-1227.

- Ihee, H.; Rajagopal, S.; Srajer, V.; Pahl, R.; Anderson, S.; Schmidt, M.; Schotte, F.; Anfinrud, P. A.; Wulff, M. & Moffat, K. (2005b). Visualizing reaction pathways in photoactive yellow protein from nanoseconds to seconds. *Proc. Natl. Acad. Sci.*, 102, 7145-7150.
- Jones, C. M.; Henry, E. R.; Hu, Y.; C.-K.Chan; Luck, S. D.; A, A. B.; Roder, H.; Hofrichter, J. & Eaton, W. A. (1993). Fast events in protein folding initiated by nanosecond laser photolysis. *Proc. Natl. Acad. Sci.*, 90, 11860-11864.
- Kainosho, M.; Torizawa, T.; Iwashita, Y.; Terauchi, T.; Ono, A. M. & P, P. G. (2006). Optimal isotope labelling for NMR protein structure determinations. *Nature*, 440, 52-57.
- Kim, C. D.; Pillet, S.; Wu, G.; Fullagar, W. K. & Coppens, P. (2002). Excited-state structure by time-resolved X-ray diffraction. *Acta Cryst. A*, 58, 133-137.
- Kim, K.-J.; Shvyd'ko, Y. & Reiche, S. (2008). A proposal for an X-ray free-electron laser oscillator with an energy-recovery linac. *Phys. Rev. Lett.*, 100, 244802.
- Kim, T. K.; Lorenc, M.; Lee, J. H.; Russo, M.; Kim, J.; Cammarata, M.; Kong, Q. Y.; Noel, S.; Plech, A.; Wulff, M. & Ihee, H. (2006). Spatiotemporal reaction kinetics of an ultrafast photoreaction pathway visualized by time-resolved liquid x-ray diffraction. *Proc. Natl. Acad. Sci. USA*, 103, 9410-9415.
- Kong, Q.; Lee, J. H.; Plech, A.; Wulff, M.; Ihee, H. & Koch, M. H. J. (2008). Ultrafast X-ray Solution Scattering Reveals an Unknown Reaction Intermediate in the Photolysis of Ru₃(CO)₁₂. *Angew. Chem. Int. Ed.*, 47, 5550-5553.
- Kong, Q. Y.; Wulff, M.; Lee, J. H.; Bratos, S. & Ihee, H. (2007). Photochemical reaction pathways of carbon tetrabromide in solution probed by picosecond X-ray diffraction. *J. Am. Chem. Soc.*, 129, 13584-13591.
- Lee, J. H.; Kim, J.; Cammarata, M.; Kong, Q.; Kim, K. H.; Choi, J.; Kim, T. K.; Wulff, M. & Ihee, H. (2008a). Transient X-ray diffraction reveals global and major reaction pathways for the photolysis of iodoform in solution. *Angew. Chem. Int. Ed.*, 47, 1047-1050.
- Lee, J. H.; Kim, K. H.; Kim, T. K.; Lee, Y. & Ihee, H. (2006). Analyzing solution-phase time-resolved x-ray diffraction data by isolated-solute models. *J. Chem. Phys.*, 125, 17450.
- Lee, J. H.; Kim, T. K.; Kim, J.; Kong, Q.; Cammarata, M.; Lorenc, M.; Wulff, M. & Ihee, H. (2008b). Capturing transient structures in the elimination reaction of haloalkane in solution by transient X-ray diffraction. *J. Am. Chem. Soc.*, 130, 5834-5835.
- Lee, S. H.; Cavalieri, A. L.; Fritz, D. M.; Swan, M. C.; Hegde, R. S.; Reason, M.; Goldman, R. S. & Reis, D. A. (2005). Generation and propagation of a picosecond acoustic pulse at a buried interface: Time-resolved X-ray diffraction measurements. *Phys. Rev. Lett.*, 95.
- Lindenau, B.; Rübiger, J.; Polachowski, S. & Fremerey, J. K. (2004). X-ray pulse selector with 2 ns lock-in phase setting and stability. *AIP Conf. Proc.*, 705, 1019-1022.
- Lindenberg, A. M.; Larsson, J.; Sokolowski-Tinten, K.; Gaffney, K. J.; Blome, C.; Synnergren, O.; Sheppard, J.; Coleman, C.; MacPhee, A. G.; Weinstein, D.; Lowney, D. P.; Allison, T. K.; Matthews, T.; Falcone, R. W.; Cavalieri, A. L.; Fritz, D. M.; Lee, S. H.; Bucksbaum, P. H.; Reis, D. A.; Rudati, J.; Fuoss, P. H.; Kao, C. C.; Siddons, D. P.; Pahl, R.; Als-Nielsen, J.; Duesterer, S.; Ischebeck, R.; Schlarb, H.; Schulte-Schrepping, H.; Tschentscher, T.; Schneider, J.; von der Linde, D.; Hignette, O.; Sette, F.; Chapman, H. N.; Lee, R. W.; Hansen, T. N.; Techert, S.; Wark, J. S.; Bergh, M.; Huldt, G.; van der Spoel, D.; Timneanu, N.; Hajdu, J.; Akre, R. A.; Bong, E.; Krejčík, P.; Arthur, J.; Brennan, S.; Luening, K. & Hastings, J. B. (2005). Atomic-scale visualization of inertial dynamics. *Science*, 308, 392-395.
- Moffat, K. (2001). Time-resolved biochemical crystallography: a mechanistic perspective. *Chem. Rev.*, 101, 1569-1581.

- Mukamel, S.; Abramavicius, D.; Yang, L.; Zhuang, W.; Schweigert, I. V. & Voronine, D. V. (2009). Coherent multidimensional optical probes for electron correlations and exciton dynamics: From NMR to X-rays. *Acc. Chem. Res.*, 42, 553-562.
- Nozawa, S.; Adachi, S.; Takahashi, J.; Tazaki, R.; Guerin, L.; Daimon, M.; Tomita, A.; Sato, T.; Chollet, M.; Collet, E.; Cailleau, H.; Yamamoto, S.; Tsuchiya, K.; Shioya, T.; Sasaki, H.; Mori, T.; Ichiyangi, K.; Sawa, H.; Kawata, H. & Koshihara, S. (2007). Developing 100 ps-resolved X-ray structural analysis capabilities on beamline NW14A at the photon factory advanced ring. *J. Synch. Rad.*, 14, 313-319.
- Plech, A.; Wulff, M.; Bratos, S.; Mirloup, F.; Vuilleumier, R.; Schotte, F. & Anfinrud, P. A. (2004). Visualizing chemical reactions in solution by picosecond x-ray diffraction. *Phys. Rev. Lett.*, 92, 125505.
- Saes, M.; Bressler, C.; Abela, R.; Grolimund, D.; Johnson, S. L.; Heimann, P. A. & Chergui, M. (2003). Observing Photochemical Transients by Ultrafast X-Ray Absorption Spectroscopy. *Phys. Rev. Lett.*, 90, 047403.
- Sato, T.; Nozawa, S.; Ichiyangi, K.; Tomita, A.; Chollet, M.; Ichikawa, H.; Fujii, H.; Adachi, S. & Koshihara, S. (2009). Capturing molecular structural dynamics by 100 ps time-resolved X-ray absorption spectroscopy. *J. Synch. Rad.*, 16, 110-115.
- Schotte, F.; Lim, M.; Jackson, T. A.; Smirnov, A. V.; Soman, J.; Olson, J. S.; Phillips, G. N. J.; Wulff, M. & Anfinrud, P. (2003). Watching a protein as it functions with 150ps time-resolved X-ray crystallography. *Science*, 300, 1944-1947.
- Schwieters, C. D.; Kuszewski, J. J.; Tjandra, N. & Clore, G. M. (2003). The Xplor-NIH NMR molecular structure determination package. *J. Mag. Res.*, 160, 65-73.
- Srajer, V.; Teng, T.-Y.; Ursby, T.; Pradervand, C.; Ren, Z.; Adachi, S.; Schildkamp, W.; Bourgeois, D.; Wulff, M. & Moffat, K. (1996). Photolysis of the carbon monoxide complex of myoglobin: Nanosecond time-resolved crystallography. *Science*, 274, 1726-1729.
- Techert, S.; Schotte, F. & Wulff, M. (2001). Picosecond X-Ray Diffraction Probed Transient Structural Changes in Organic Solids. *Phys. Rev. Lett.*, 86, 2030-2033.
- Tomita, A.; Sato, T.; Ichiyangi, K.; Nozawa, S.; Ichikawa, H.; Chollet, M.; Kawai, F.; Park, S.-Y.; Tsuduki, T.; Yamato, T.; Koshihara, S. & Adachi, S. (2009). Visualizing breathing motion of internal cavities in concert with ligand migration in myoglobin. *Proc. Natl. Acad. Sci. USA*, 106, 2612-2616.
- Vincent, J.; Andersson, M.; Eklund, M.; Wohri, A. B.; Odelius, M.; Malmerberg, E.; Kong, Q. Y.; Wulff, M.; Neutze, R. & Davidsson, J. (2009). Solvent dependent structural perturbations of chemical reaction intermediates visualized by time-resolved x-ray diffraction. *J. Chem. Phys.*, 130, -.
- Wall, M.; Tarnovsky, A. N.; Pascher, T.; Sundstrom, V. & Akesson, E. (2003). Photodissociation Dynamics of Iodoform in Solution. *J. Phys. Chem. A*, 107, 211-217.
- Wulff, M.; Bratos, S.; Plech, A.; Vuilleumier, R.; Mirloup, F.; Lorenc, M.; Kong, Q. & Ihee, H. (2006). Recombination of photodissociated iodine: A time-resolved x-ray-diffraction study. *J. Chem. Phys.*, 124, 034501.
- Wulff, M.; Schotte, F.; Naylor, G.; Bourgeois, D.; Moffat, K. & Mourou, G. (1997). Time-resolved structures of macromolecules at the ESRF: Single-pulse Laue diffraction, stroboscopic data collection and femtosecond flash photolysis. *Nucl. Instrum. Methods*, A398, 69-84.
- Zheng, X. M. & Phillips, D. L. (2000). Solvation effects on the iodoform ultraviolet direct photodissociation reaction. opening the photoisomerization channel. *Chem. Phys. Lett.*, 324, 175-182.